Available online at www.sciencedirect.com

jmr&t Journal of Materials Research and Technology

journal homepage: www.elsevier.com/locate/jmrt

Original Article

# Design of graphene-based multi-parameter sensors

*Fengjuan Miao* [a,1,*], *Yue Han* [a,1], *Jinxin Shi* [a,1], *Bairui Tao* [a,**], *Peng Zhang* [a,***], *Paul K. Chu* [b]

[a] *College of Communications and Electronics Engineering, Qiqihar University, Heilongjiang 161006, China*
[b] *Department of Physics, Department of Materials Sciences and Engineering, and Department of Biomedical Engineering, City University of Hong Kong, Tat Chee Avenue, Kowloon, Hong Kong, China*

ARTICLE INFO

*Article history:*
Received 13 June 2022
Accepted 26 December 2022
Available online 29 December 2022

*Keywords:*
Graphene-based
Low-cost
Multidimensional sensor
Agricultural sensors

ABSTRACT

Agricultural informatization, modernization is an important development trend of agriculture, and building low-cost agricultural sensors has become a hot topic. In this paper, a multi-parameter preparation method suitable for agricultural information technology based on graphene and its doped-modified nanocomposites is proposed. The nanomaterials such as zinc oxide, titanium dioxide, stannic oxide, and molybdenum disulfide were synthesized by hydrothermal method, combined with graphene to prepare sensors. The finally completed graphene multi-parameter sensor is suitable for the agricultural environment, the temperature measurement ranges from 10 to 60 °C, the light intensity measurement ranges from 1000 to 11,000 lux, the humidity measurement ranges from 11% to 97 %RH, and the 300–1100 ppm $CO_2$ concentration measurement range, and the response time is short. The material used is low, cost-effective, and the measurement parameters make it a suitable agricultural sensor, which will bring a large economic and social value, lay the foundation for the agricultural sensor to meet market needs.



## 1. Introduction

With the continuous development of agricultural technology, the requirements for agricultural information collection are becoming higher and higher [1–3]. The problem that occurs is that the performance of the multi-sensor has gradually discovered that the use scenarios of the most sensors are symbiotic [4]. If a plurality of sensors is combined together, it can not only reduce the cost of the sensor, but simplify the flow of data acquisition [5,6]. Wajid A et al. constructed a new organic semiconductor temperature and humidity sensor with Ag/$SnNcCl_2$/Ag, which has a short response and recovery time, which can be applied to daily practice, but the material is not suitable for large-scale

* Corresponding author.
** Corresponding author.
*** Corresponding author.
E-mail addresses: miaofengjuan@163.com (F. Miao), tbr_sir@163.com (B. Tao), zhangpeng@qqhru.edu.cn (P. Zhang).
[1] Fengjuan Miao, Yue Han and Jinxin Shi are co-first authors.
https://doi.org/10.1016/j.jmrt.2022.12.157

promotion [7]. Karimov K S et al. prepared elastic lamellar rubber-graphene composites by friction method to construct displacement, pressure, humidity and temperature sensors, and found that the composite materials have broad application prospects in displacement, frequency, temperature and pressure sensors [8]. The performance comparison between the sensor studied in this paper and the existing sensor is shown in Table 1. The corresponding sensitive materials are modified between the electrodes, the dielectric constant of the electrodes is changed, and the capacitance and resistance of the sensor are changed. It is found that metal oxides [9–12] such as zinc oxide (ZnO), titanium dioxide ($TiO_2$), stannic oxide ($SnO_2$), and molybdenum disulfide ($MoS_2$) have good sensitivity to temperature, light intensity, humidity and carbon dioxide, respectively. These metal oxides are modified on the electrode surface as corresponding sensitive materials, resulting in changes in electrode capacitance or resistance. The addition of graphene (G) can improve the sensitivity of the parameters [13–15], so the preparation and application of G and metal oxide binding have attracted extensive attention in recent years. Multi-parameter sensors are applicable to many ways, and in various research areas, it can be used to monitor temperature and liquid leakage [16], glucose and pH value detection [17], temperature and humidity and photodetector multi-function sensors [18], etc. From the perspective of scientific research and practical applications, multiple sensors can be used to better apply the actual situation of agricultural monitoring, making it more convenient to use the Internet of Things technology to agriculture.

In this work, a graphene-based Multi-parameter sensor with resistance and capacitance as variable is designed and realized by using hydrothermal method to prepare sensitive materials and multidimensional sensor integration technology. In this paper, ZnO, $TiO_2$, $SnO_2$ and $MoS_2$ are used as sensitive materials to prepare temperature-sensitive, humidity-sensitive, light-sensitive and gas-sensitive multi-dimensional sensors by thermal transfer printing technology. The four sensors are integrated together to form a multi-parameter sensor, which greatly reduces the manufacturing cost of the sensor; and the use of metal oxides as a sensitive material can not only be quickly deployed in comprehensive applications, but also beneficial to agricultural informatization and modernization.

## 2. Experimental section

### 2.1. Experimental reagent

All reagents were analytical without purification. $Zn(NO_3)_2 \cdot 6H_2O$, $Zn(CH_3COO)_2 \cdot 2H_2O$, $(NH_4)_6Mo_7O_{24} \cdot 4H_2O$, $CH_4N_2S$, $CH_3COOK$, $K_2CO_3$, KCL were purchased from Tianjin Keemi Chemical Reagent Co., Ltd. ($C_6H_{12}N_4$) Hengxing Chemical Reagent Manufacturing Co., Ltd., $SnCl_4 \cdot 5H_2O$, purchased from Tianjin Dongli District Tianda Chemical Reagent Factory; $TiO_2$ is purchased from Aladdin Reagent (Shanghai) Co., Ltd.; LICL, $CuSO_4$ is purchased from Tianjin Kaisong Chemical Reagent Co., Ltd. NaOH $C_2H_5OH$ was purchased from Tianjin Tianli Chemical Reagent Co., Ltd.

### 2.2. Preparation of sensor materials

#### 2.2.1. A: Synthesis of ZnO nanomaterials

0.74 g of $Zn(NO_3)_2 \cdot 6H_2O$, 1.08 g of hexamethylenediamine was mixed with 50 ml of deionized water and ultrasonic treatment for 30 min to form a homogeneous solution. Transfer it into the PTF liner in the high-pressure sterilizer, and the high-pressure sterilizer was heated to a 95 °C environment for 5 h for water heat treatment to form a nano-zinc oxide solution. After cooling to room temperature, the prepared solution was placed in a centrifuge and centrifuged at 5000–10,000 rpm for 5–10 min. The resulting precipitate was allowed to separate the resulting precipitate in a large amount of water-free ethanol and deionized water after centrifugation. The precipitate was finally rinsed with deionized water, dried under 60 °C for 12 h to obtain white nano-zinc oxide powder. The preparation process of nanomaterials is shown in Fig. 1.

#### 2.2.2. B: Synthesis of $TiO_2$ nanomaterials

Mix 0.5 g of commercial titanium dioxide powder with 20 g of NaOH aqueous solution and absolute ethanol in a volume ratio of 1:1. The mixed solution of 20 ml was transferred in the stainless-steel autoclave, and the autoclave was heated to 200 °C under the environment to carry out hydrothermal treatment and maintained for 24 h to generate titanium dioxide nano-solution. After cooling to room temperature, the prepared solution is sampled and filtered, placed in a centrifuge and centrifuged at a rotational speed of 5000–10,000 rpm,

**Table 1 – Compare with other sensors.**

| Material | The preparation process | Scope of application | Test Range | Res and Rec Time | Ref |
|---|---|---|---|---|---|
| Graphene and P(VDF-TrFE) | Sonochemical approach | Large | −20 - 300 °C | 4 s and 3 s | [19] |
| MWCNTs | Knife-over-roll coating technique | Small | 200–700 °C | – | [20] |
| MWCNTs | Knife-over-roll coating technique | Small | 60% - 90 %RH | 4 s and 30 s | [20] |
| $WS_2$ | deposition | Large | 8% - 85 %RH | 140 s and 30 s | [21] |
| $WS_2$ | Films were deposited | Small | – | 5–10 s and - | [22] |
| Fluoropolymer thin film | Dry application | Large | 420–2000 ppm | 40 s and 20 s | [23] |
| ZnO/G | Hydrothermal method | Small | 10–60 °C | 12 s and 8 s | Our work |
| $SnO_2$/G | | Large | 11 - 97 %RH | 16 s and 7 s | |
| $TiO_2$/G | | Large | 1000–11000 lux | 6 s and 2 s | |
| $MoS_2$/G | | Large | 300–1000 ppm | 47 s and 83 s | |

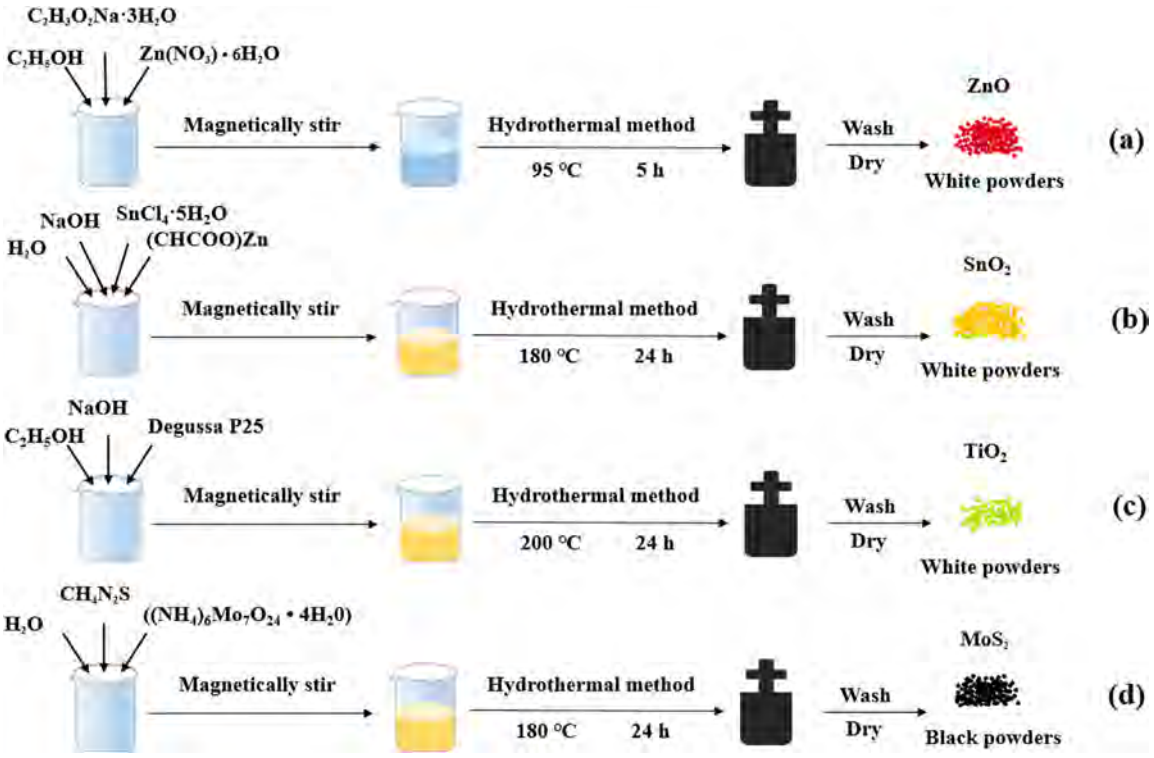


**Fig 1 – (a)–(d) Schematic diagrams of the fabrication flow of different sensitive materials.**

and the centrifugation time is 5–10 min. The precipitate was washed with dilute aqueous hydrochloric acid and deionized water until the pH of the solution was adjusted to around 7. Nanowire-like titanium dioxide white powder can be prepared by drying at 60 °C for 12 h.

#### 2.2.3. C: Synthesis of $SnO_2$ nanomaterials

Synthesis of $SnO_2$ by utilizing hydrated tin chloride ($SnCl_4$ $5H_2O$) and sodium hydroxide (NaOH), and zinc acetate was used to adjust the pH value of the reaction solution to modify the morphology of $SnO_2$. Then, 0.7 g of hydrated tin chloride, 0.6 g of sodium hydroxide, and 0.05 g of zinc acetate were added to a mixed solution consisting of 15 ml of absolute ethanol and deionized water in a volume ratio of 1:1, by magnetic stirring method. The solute is fully dissolved in the solvent to form a milky white homogeneous solution. The homogeneously stirred milky white solution is transferred in the stainless-steel autoclave, and the autoclave is heated to 180 °C under the environment to carry out hydrothermal treatment for 24 h to generate nano-tin oxide solution. After cooling to room temperature, the prepared solution was placed in a centrifuge at 5000–10,000 rpm and centrifuged for 5–10 min. After standing and separating the obtained precipitate, rinse the precipitate with deionized water, and dry it at 60 °C for 12 h to obtain white tin oxide powder.

#### 2.2.4. D: Synthesis of $MoS_2$ nanomaterials

The Mo source and S source selected to synthesize $MoS_2$ are: ammonium molybdate ($(NH_4)_6Mo_7O_{24}·4H_2O$) and thiourea ($CH_4N_2S$). Mix 0.3 g of $(NH_4)_6Mo_7O_{24}·4H_2O$ and 0.2 g of $CH_4N_2S$ in 40 ml of deionized water, and place the resulting mixture on a magnetic stirrer for full stirring until all the solutes are dissolved to obtain a transparent solution. The above transparent solution was transferred to the stainless-steel high-pressure sterilizer with Teflon lining, and the high-pressure sterilizer was heated to 180 °C for 24 h to generate nano-molybdenum disulfide solution. After cooling to room temperature, the prepared solution was sampled and filtered, placed in a centrifuge at 5000–10,000 rpm and centrifuged for 5–10 min, and the resulting precipitate was left to stand for separation. Finally, the precipitate is washed with deionized water, and dried at 60 °C for 12 h to obtain black nano-molybdenum disulfide powder.

### 2.3. Materials characterization

The morphology and microstructure of the materials were characterized by scanning electron microscopy (SEM, Tescan MIRA 3XMU), transmission electron microscopy (TEM, JEM 2100F). Energy-dispersive X-ray spectrometry (EDS, JEOL JSM-7800F) and X-ray photoelectron spectroscopy (XPS, ESCA-LAB250XI) were conducted to determine the composition and chemical states. X-ray diffraction (XRD, DIFFRACTOMETER-6000) was carried out to determine the phases of the materials.

### 2.4. Experimental principle

In this paper, the sensors are divided into two types: resistive sensors and capacitive sensors. Among them, temperature sensitive sensors and light sensitive sensors are resistive sensors; humidity sensors and gas sensors are capacitive

sensors. Resistive sensors are made using the physical property that resistance changes with parameter changes. The resistivity of a conductor or semiconductor is related to the number of electrons involved in the conduction process, the crystal structure and its state in the material, and they have different conduction mechanisms. The resistivity of the conductor can be known according to Ohm's law:

$$\rho = \frac{E}{J}$$

In the formula: $E$ represents the electric field strength; $J$ represents the current density. At the same time, under the action of the electric field strength $E$, the value of the current density $J$ is proportional to the electric charge $E$, the number of free electrons n and the directional velocity u of the electrons. For metal conductors, the resistivity and resistance of a substance have a clear mathematical function relationship:

$$R = \rho \frac{l}{s}$$

In the formula: $R$ represents the conductor resistance, $l$ represents the conductor length, and s represents the conductor cross-sectional area. At this time, the influence of parameters on resistivity is fed back to the resistance, that is, parameter changes will lead to resistance changes. A semiconductor is a crystalline solid with a special atomic structure. When the electrons in the outer layer move, they are neither easily separated from the original track like a metal conductor nor tightly bound like an insulator. This determines that its electrical conductivity is between that of a metal conductor and an insulator. The conduction mechanism is related to the valence electrons in the material and the doped impurities. Due to the influence of doping degree and manufacturing process, it is difficult to give a unified equation to describe the resistance characteristics of semiconductors. The typical empirical formula is:

$$R = B \times e^{\frac{\Delta E}{2kT}}$$

In the formula, the coefficient B depends on the formula, the coefficient $B$ depends on the type and concentration of doping, and changes with the parameters; $\Delta E$ is related to the forbidden bandwidth, and k is the Boltzmann constant.

Generally, the electrical resistance of conductive nanocomposites will change with the change of ambient temperature, a phenomenon known as thermal resistance effect or thermosensitive effect. In recent years, many researchers have studied the mechanism leading to this phenomenon. At present, the main mechanisms to explain the thermal resistance effect are thermal expansion theory and tunnel effect theory. The thermal expansion theory believes that this thermal resistance effect of conductive composites is caused by the different thermal expansion coefficients of matrix materials and conductive fillers. The theory incorporates conductive chains to explain the thermal resistance effect. It is believed that the conductive behavior of the composite material is caused by the conductive chains formed by the conductive fillers in the system. When the ambient temperature rises, the spacing of the conductive fillers increases, and the conductive chains are destroyed and the system resistance increases, resulting in a positive temperature coefficient of the conductive composites. Direction of development. The thermal expansion theory can usually only be used to explain the PTC effect, and it is difficult to explain the phenomenon that the resistance decreases with increasing temperature. The temperature-sensitive sensor uses ZnO/G as the temperature-sensitive material. When the temperature in the environment increases, ZnO is thermally expanded, changing its dielectric constant, which in turn affects the change of resistance; the relationship between the two is that with the continuous increase of temperature, the resistance decreases.

The photosensitive sensor uses $TiO_2$ as an ultraviolet light sensor. The research is also based on the selective absorption of ultraviolet light and its photovoltaic properties of $TiO_2$, and the photoconductive effect and photovoltaic effect generated by the wide band gap semiconductor $TiO_2$ after absorbing ultraviolet light. But the goal is not to capture the energy it converts, but to detect the intensity of the UV light signal received by the $TiO_2$ in turn by measuring the electrical signal (photogenerated current, photogenerated voltage, or photoconductance) converted by the $TiO_2$. In addition, the use of $TiO_2$ materials to make ultraviolet light sensors has low cost, relatively simple process, excellent anti-interference, weather resistance, chemical stability and other properties, and has extensive and important application prospects.

It is well known that capacitance is expressed as:

$$C = \frac{\varepsilon_0 \varepsilon_r A}{d}$$

where $\varepsilon_0$ is the dielectric constant in vacuum, $\varepsilon_r$ is the relative dielectric constant, A is the electrode area, and d is the distance between the electrodes, that is, the thickness of the dielectric layer. Humidity sensors are the best known capacitive sensors. The working principle of capacitive humidity sensor is to use sensitive materials to adsorb water molecules, material dielectric constant changes caused by capacitance changes, the basic structure is to build a film with good water permeability on the substrate as a conductive layer, increase polymer moisture film as a sensitive layer, this paper uses G as a conductive material, $SnO_2$ as a sensitive material to construct a capacitive humidity sensor [24]. As the humidity of the external environment increases, the electrode constructs a chemisorption layer as a substrate, and a physical adsorption layer is generated on the chemisosorption layer to adsorb water molecules, and $H_3O^+$ is generated as a carrier when the electrostatic field is ionized [25]. As the water molecules are ionized under the electrostatic field, $H_3O^+$ will be generated as a charge carrier. As the adsorption process of water molecules continues, the multi-layer physical adsorption of water molecules exhibits a liquid-like behavior, that is, the protons induced by $H_2O + H_3O^+ = H_3O^+ + H_2O$ migrate through ionic conductivity hopping. Under high RH conditions, free water can penetrate into the interlayer of $SnO_2$ films, which greatly improves the dielectric constant and sensor response.

Metal oxide semiconductors have become one of the most promising gas sensor materials due to their high sensitivity, fast response, long lifetime and low cost. $MoS_2$ with a graphene-like structure has good electrical conductivity, large

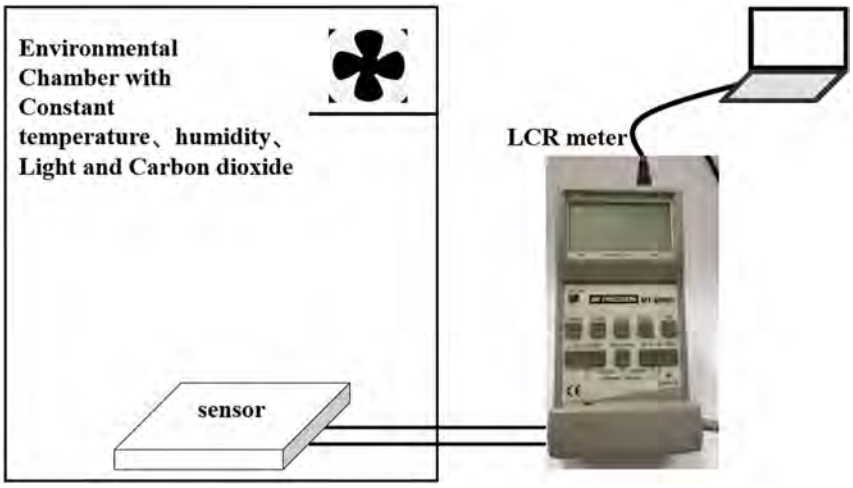


**Fig 2 – Schematic diagram for sensor test.**

specific surface area, good stability, $MoS_2$ has attracted much attention due to its strong adsorption and high reactivity. $MoS_2$ has good electrical conductivity and large specific surface area. When the gas is absorbed into the micropores of the permeable solid, the effective dielectric constant of the film/gas is similar to that of the film in vacuum, When $CO_2$ gas is absorbed into the micropores of permeable solids, the effective permittivity of the film/gas differs from the dielectric constant of the thin film in a vacuum [26]. We start with the Clausius-Mosotti formula, which gives the relationship between the permittivity of each phase and its polarizability:

$$P=\frac{\varepsilon-1}{\varepsilon+2} \text{ or } \varepsilon=\frac{2P-1}{1-P}$$

In the formula, $P$ is the polarizability (the proportionality constant is the molar volume). When used in a gas-solid mixture, the polarizability of the gas-solid two phases is additive (provided that the gas-solid two-phase separation is maintained), as can be seen from the following formula:

$$\varepsilon_{s+g}=\frac{2P_s+2P_g+1}{1-P_s-P_g}$$

The difference in permittivity $\Delta\varepsilon$ is defined as $\varepsilon_{s+g}-\varepsilon_s$ and can be expressed as:

$$\Delta\varepsilon=\frac{3P_g}{1-P_g+P_gP_s-2P_s+P_gP_s}$$

After eliminating $P_g$ in the denominator under the limit of $P_g \ll P_s < 1$;

$$\Delta\varepsilon\approx\frac{3P_g}{(1-P_s)^2}$$

Using Equation $1-P_s=\frac{3}{\varepsilon_s+2}$, the above formula can be reduced to the limit of $\varepsilon_g \to 1$ as:

$$\Delta\varepsilon=\frac{(\varepsilon_g-1)(\varepsilon_s+2)^2}{9(1-P_s)^2}$$

Standard values for $\varepsilon_g$ are usually provided at 1 atm pressure and one standard temperature, using the values of $\varepsilon_g-1$ for $CO_2$ and air, 922 and 536 ppm, respectively, with a correction for the measured $CO_2$ to affect the change in dielectric constant by carbon dioxide in the gas phase This in turn causes a change in capacitance.

### 2.5. *Measurement environment*

Taking the JKZ1 radiosonde detection box (Shanghai Changwang Meteorological Technology Co., Ltd.) as the closed environment, different environmental parameters are obtained by controlling the environmental parameters in the closed box such as temperature, light, humidity, $CO_2$, by the radiosonde. The sensor data measurement uses the MT4080A LCR meter. The resistance and capacitance of the test electrodes are transmitted to the computer through the LCR meter, and are compared with the calibrated parameters and then converted into the tested environmental parameter values. The measurement environment is shown in Fig. 2. At the same time, in the preparation of the sensitive electrode, the sensitive material and graphene are sequentially coated by a spin coater, so that they are covered on the electrode, and related performance tests are carried out.

## 3. Results and discussion

### 3.1. *Structural and morphological studies*

It can be seen from supporting material 1 that the ZnO prepared in this paper presents nanorods. From supporting material 1(a) SEM, it can be seen that the structure is hexagonal prism. The uniform hexagonal prism structure of nanorods is beneficial to the change of dielectric constant of ZnO. The combination of ZnO and graphene increases the spatial structure of the electrode as a whole. The modification of graphene makes the sensitive material more sensitive to the change of temperature [27]. In supporting material 1(b), we can clearly distinguish the nanorod-like ZnO and sheet graphene structure at high magnification. At the same time, it

can be seen in the microscopic situation that the submicron structure of nanomaterials is less than 0.2 μm, and its morphology is corresponding to that of SEM. It can be seen from EDS spectrum characterization supporting material 1(c) that the content of Zn in the sensitive material is the highest, indicating that the theme of the prepared material is ZnO, followed by C content, which is modified by ZnO graphene. From supporting material 1(f), it can be seen that ZnO and Zn elements correspond to nanorods, while graphene and C elements correspond to sheet structure, which corresponds to the previous SEM and TEM. The XRD spectra of ZnO/G are shown in supporting material 1(d), and the crystal structure and composition of the sensitive materials are characterized. The diffraction peaks of ZnO (JCPDS No.89-0511) at 2θ in ZnO/G are at 31.78°, 34.43°, 36.26°, 47.56°, 56.61°, 62.87° and 67.96°, corresponding to the ZnO planes of (100), (002), (101), (102), (110), (103) and (112), respectively. The diffraction value of graphene (JCPDS No.26–1080) at 2θ is 26.60°, and the corresponding crystal plane is (002). The peak height is determined by the number of crystal planes. The higher the peak value, the higher the material content, the intensity of the peak can also be regarded as the content of the material. Usually, the stronger the peak, the higher the material content. The chemical composition and valence state of elements on the surface of nanomaterials can be further understood by XPS analysis. The XPS spectra are shown in supporting material 1(e), showing the presence of Zn, O and C elements in ZnO/G nanocomposites, which corresponds to the EDS results. The valence states of these elements in nanocomposites were studied. The binding energies of 1021.4 eV and 1045.1 eV are attributed to $Zn2p_{1/2}$ and $Zn2p_{3/2}$, respectively, as shown in the figure, indicating that $Zn^{2+}$ exists in the ZnO/G sensitive electrode nanocomposites. O1s is the two oxygen supply peaks of high-resolution spectral decomposition, and the peak at 531.4 eV is generated by $O^{2-}$ in the Zn–O band. The three-dimensional spectrum of C is shown in the figure. The spectrum of C is shown in the figure. The peaks at 285.11 eV are C1s, and its splitting is about 287.65 eV, which is the characteristic peak of C. XPS results showed that ZnO/G nanocomposites were formed on the substrate.

Solvent is an important factor that determines the crystal morphology, solvents with different physical and chemical properties will affect the solubility, reactivity and diffusion behavior of reactants; in particular, the polarity and coordination ability of the solvent will affect the morphology and crystallization behavior of the final product [28]. The existence of high concentration ethanol not only causes the change of solvent polarity, but also strongly affects the potential value of reactant particles and the increase of solution viscosity. For example, in the absence of ethanol, a short and wide sheet of titanium dioxide structure, rather than nanowires, was obtained. When chloroform was used, $TiO_2$ nanorods were obtained. Supporting material 2(a,b) are representative SEM and TEM images of $TiO_2$ nanowires prepared by solvothermal method. It can be seen from the figure that the prepared $TiO_2$ is linear. Compared with particles and flakes, linear $TiO_2$ has better performance and is more sensitive to light. It can be seen from the EDS energy spectrum characterization supporting material 2(c) that the content of Ti in the sensitive material is the highest, indicating that the theme of the prepared material is $TiO_2$, followed by the content of O, and the third is graphene modified by C element. From supporting material 2(f), it can be seen that $TiO_2$ and Ti elements correspond to nanowires, while graphene corresponds to C elements in a sheet-like structure, which echoes the SEM and TEM described above. The XRD spectrum of $TiO_2$/G is shown in supporting material 2(d), which characterizes the crystal phase structure and composition of the sensitive material. The diffraction peaks of $TiO_2$/G at 2θ are at 27.45°, 36.09°, 39.19°, 41.23°, 44.05°, 54.32°, 56.64°, 62.74°, 64.04°, 69.01° and 69.79°, which correspond to the tetragonal $TiO_2$ structure (JCPDS No. 21–1276) of (110), (101), (200), (111), (210), (211), (220), (002), (310), (301) and (112) phases [29]. The diffraction value of graphene (JCPDS No. 26–1080) at 2θ is 26.60°, and the corresponding crystal plane is (002). Supporting material 2(e) is the XPS spectrum of the sensitive material, which proves that there are signals related to Ti, O and C in the material. The first one in the figure is the full spectrum of $TiO_2$. The Ti spectrum reveals the existence of two signals: the first at 457.9 eV and the second at 463.5 eV, corresponding to the $2p_{3/2}$ and $2p_{1/2}$ orbital energy levels, which are due to the spin-orbit coupling effect, which can be attributed to the binding energy difference is 5.6 eV due to $Ti^{4+}$ [30]. Among them, the mathematical analysis of the Ti2p region shows that the $Ti^{4+}$ and $Ti^{3+}$ signals appear at the same location, which indicates that both oxidation states of titanium actually exist in the composite. The XPS spectrum of O 1s in the figure shows that the lattice of the material is modified. Which consists of three signals: the first peak at 529.0 eV is attributed to oxygen vacancies, and the next peak at 530.7 eV is attributed to Ti–O Order in the lattice (i.e., lattice oxygen). The C spectrum shows three signals: 283.30 eV corresponds to the C–C bond, and 287.8 eV can be explained by the interaction of surface carbon and oxygen.

The $SnO_2$ synthesized by hydrothermal method is white powder. Supporting material 3(a) shows the morphology and structure characteristics of $SnO_2$. It can be seen that the synthesized $SnO_2$ is a uniform nanosphere structure, and the surface of each sphere is covered with slender and highly ordered nanoneedles. This structure leads to the loose structure of the synthesized $SnO_2$ nanostructures and has a larger specific surface area. It is convenient for $SnO_2$ molecules to contact with water molecules in the external air and carry out efficient electronic transmission in the process of humidity detection. Supporting material 3(b) shows the needle-like morphology of $SnO_2$ and the sheet structure of graphene more clearly. In the EDS spectrum characterization supporting material 3(c), it can be seen that the content of Sn in the sensitive material is the highest, indicating that the theme of the prepared material is $SnO_2$, followed by O content, and the third is C element modified $SnO_2$ graphene. From supporting material 3(f), it can be seen that $SnO_2$ and Sn correspond to the nanosphere morphology, while graphene corresponds to the lamellar structure of C element, which corresponds to the SEM and TEM in the previous paper. The XRD spectra of $SnO_2$/G are shown in supporting material 3(d), and the crystal structure and composition of the sensitive materials are characterized. The diffraction peaks of $SnO_2$/G at 2θ are at 26.6°, 33.8°, 37.9°, 51.7°, 54.7°, 61.8° and 78.7°, respectively corresponding to (110), (101), (200), (211), (220), (310) and (321) phases of

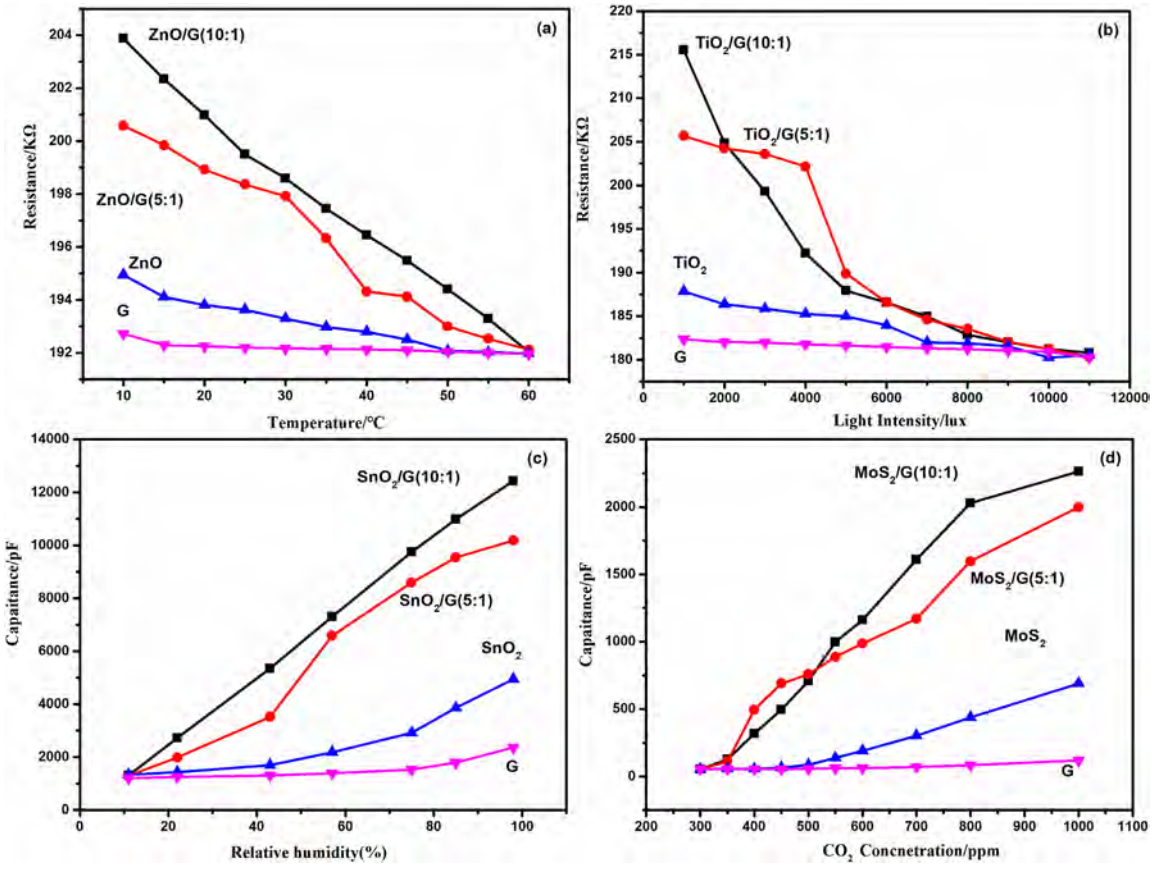


**Fig 3 – (a) Comparison of temperature-sensitive materials; (b) Comparison of photosensitive materials; (c) Comparison of humidity-sensitive materials; (d) Comparison of gas-sensitive materials.**

tetragonal $SnO_2$ structure (JCPDS No.41–1445) [31,32]. The diffraction value of graphene (JCPDS No.26–1080) at 2θ is 26.60°, and the corresponding crystal plane is (002). The chemical composition and valence state of elements on the surface of nanomaterials can be further understood by XPS analysis. The XPS spectra are shown in supporting material 3(e), showing the existence of Sn, O and C elements in $SnO_2$/G nanocomposites, which corresponds to the EDS results. The valence states of these elements in nanocomposites were studied. The binding energies of 496.64 eV and 487.31 eV are attributed to Sn3d5, respectively, as shown in the figure, indicating that $Sn^{2+}$ exists in the $SnO_2$/G sensitive electrode nanocomposites. O1s is the two oxygen supply peaks of high-resolution spectral decomposition, as shown in the figure. The peak at 531.74 eV is generated by the $O^{2-}$ in the Sn–O band. The spectrum of C is shown in the figure. The peaks at 284.33 eV are C1s. XPS results show that $SnO_2$/G nanocomposite is formed on the substrate.

The $MoS_2$ synthesized by the hydrothermal method has a black powdery structure with fluffy silty. The topographic images shown in supporting material 4(a) and supporting material 4(b) demonstrate the morphological and nanostructural features of $MoS_2$ powders at different magnifications. It can be seen that the $MoS_2$ synthesized by this method has a cauliflower-shaped nano-flower-like structure, and the diameter of each nano-curd is about 300 nm, and each curd is formed by the interconnected combination of curled and folded nano-sheets. This structure leads to a loose $MoS_2$ nanostructure and a larger specific surface area, which facilitates the contact between $MoS_2$ molecules and gaseous molecules in the outside air during the $CO_2$ detection process for efficient electron transport. In supporting material 4(c), it can be seen that the content of Mo in the sensitive material is the highest, indicating that the theme of the prepared material is $MoS_2$, followed by graphene whose C content is modified $MoS_2$. From supporting material 4(f), it can be seen that $MoS_2$ and Mo elements correspond to the nanoflower shape, while graphene corresponds to the C element in a sheet-like structure, which echoes the formation of SEM and TEM in the previous article [33]. In order to characterize the crystallization of the composites, the $MoS_2$/G composites were tested by XRD. The test results are shown in supporting material 4(d), where the diffraction peaks at 2θ at 14.53°, 33.03°, 34.06°, 38.370°, 41.11°, 48.13°, 58.32°, 60.50° and 76.15° correspond to $MoS_2$(JCPDS No. 17–0744) and the corresponding crystal planes of the characteristic diffraction peaks are (003), (101), (012), (104), (015), (107), (110), (113) and (119) [34]. The diffraction value of graphene (JCPDS No. 26–1080) at 2θ is 26.60°, and the corresponding crystal plane is (002). To further understand the chemical composition and valence state of its surface elements, XPS analysis was performed. The XPS spectrum is shown in supporting material 4(e), which shows the presence of Mo, S, and C elements in the $MoS_2$/G nanocomposite, which corresponds to the EDS results. The valence states of these

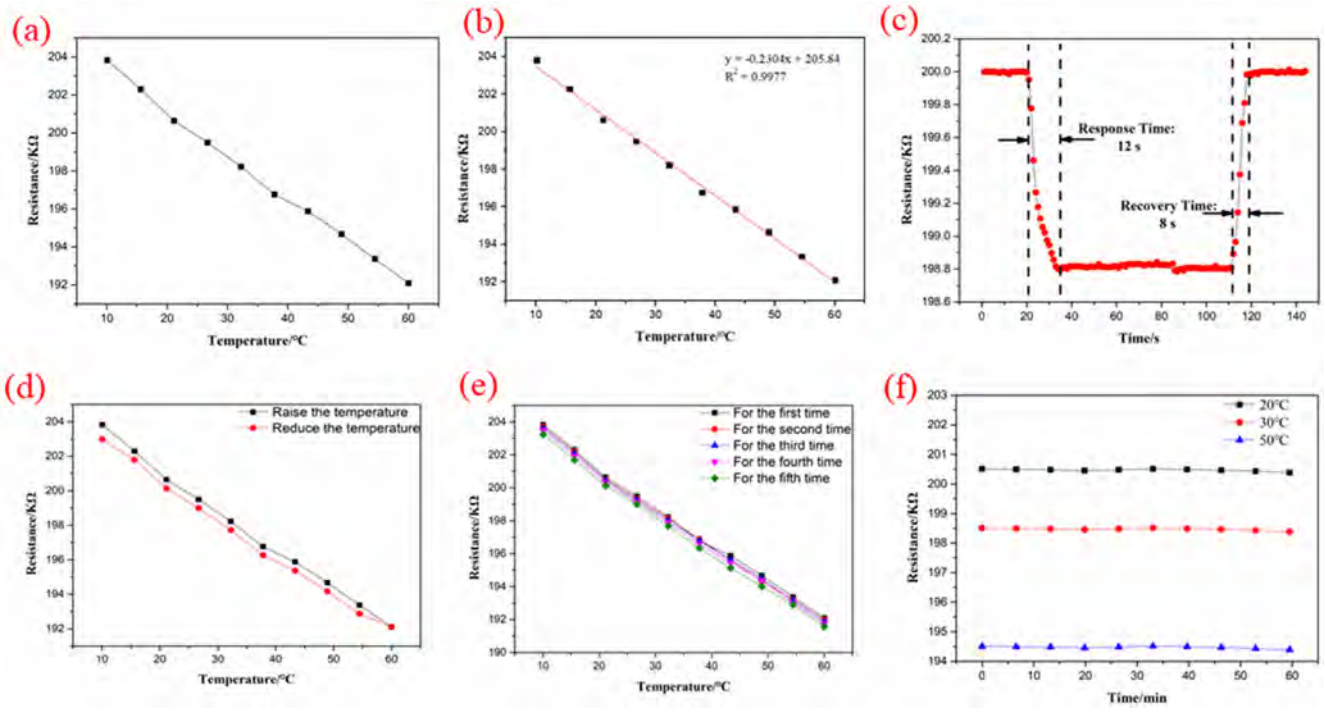


**Fig 4 – (a) Resistance characteristic diagram of temperature-sensitive sensor; (b) data fitting diagram of temperature-sensitive sensor; (c) response and recovery time test diagram; (d) temperature hysteresis test diagram; (e) repeatability test diagram; (f) stability test picture.**

elements in nanocomposites were investigated. The binding energies of 228.64 eV and 232.31 eV are assigned to $Mo3d_{3/2}$ and $Mo3d_{5/2}$, respectively, corresponding to $Mo^{6+}$, S2p is the two peaks of high-resolution spectral decomposition as shown in the figure, the peaks at 162.1 eV and 163.0 eV correspond to $2p_{3/2}$ and $2p_{1/2}$. The three-dimensional spectrum of C is shown in the figure, the peaks at 285.11 eV are respectively C1s. The results of XPS spectra indicated that $MoS_2$/G nanocomposites were formed on the substrate.

### 3.2. *Testing and analysis*

The graphene required for this experiment was purchased from Lifestar Nanotechnology. The temperature-sensitive material selected in this paper is ZnO/G. During the test, the temperature-sensitive properties of ZnO, G, ZnO/G (5:1) and ZnO/G (10:1) were tested respectively. The results are shown in the Fig. 3(a), it can be seen that ZnO/G (10:1) has good temperature-sensitive properties. The sensing performance of the temperature sensor prepared by ZnO/G composite was tested, and the test results are shown in Fig. 4. It can be considered that the temperature sensing mechanism of the device is that when the external temperature increases, the volume of ZnO will have a very small thermal expansion, which leads to the polarization of ZnO nanorods. The polarized electric field promotes the charge separation and enters the circuit, resulting in the decrease of the resistance in the circuit. Fig. 4(a) shows the curve of the resistance of the prepared electrode as a function of temperature. It can be seen from the figure that the ZnO/G thermistor has a certain conductivity, and the resistance value is in the order of $10^4$. The thermistor of pure ZnO is larger, about $10^8$ orders of magnitude, indicating that graphene plays a role in improving the conductivity of the thermistor. As the temperature increases, the resistance of the ZnO/G composite decreases gradually. It can be seen from the figure that the change of the resistance of the electrode in unit degrees Celsius has a consistent trend with the temperature change, and the basic coincidence presents a linear relationship, indicating that the ZnO/G temperature sensor has practical application potential. Fig. 4(b) is the fitting graph of the temperature-sensitive sensor data, the fitting formula is $y = -0.23x+205.84$, and the correlation coefficient $R^2 = 0.9977$. Fig. 4(c) is the response time diagram of the temperature sensitive resistance sensor. As the temperature increases, the spacing between temperature-sensitive materials increases, causing changes in the dielectric constant, and eventually a change in the resistance value. When the temperature rises from 25 °C to 30 °C at normal temperature, the response time is 12 s and the recovery time is 8 s. Because this is the transition from normal to high temperature, the response time is longer than recovery time [35]. Fig. 4(d) shows the temperature hysteresis characteristics of the ZnO/G composite temperature sensor. The resistance change curve of the experiment is taken for comparison. The square icon represents the heating process, and the circular icon represents the cooling process. It can be seen from the figure that the resistance of the temperature sensor changes regularly in the process of heating and cooling, and it is

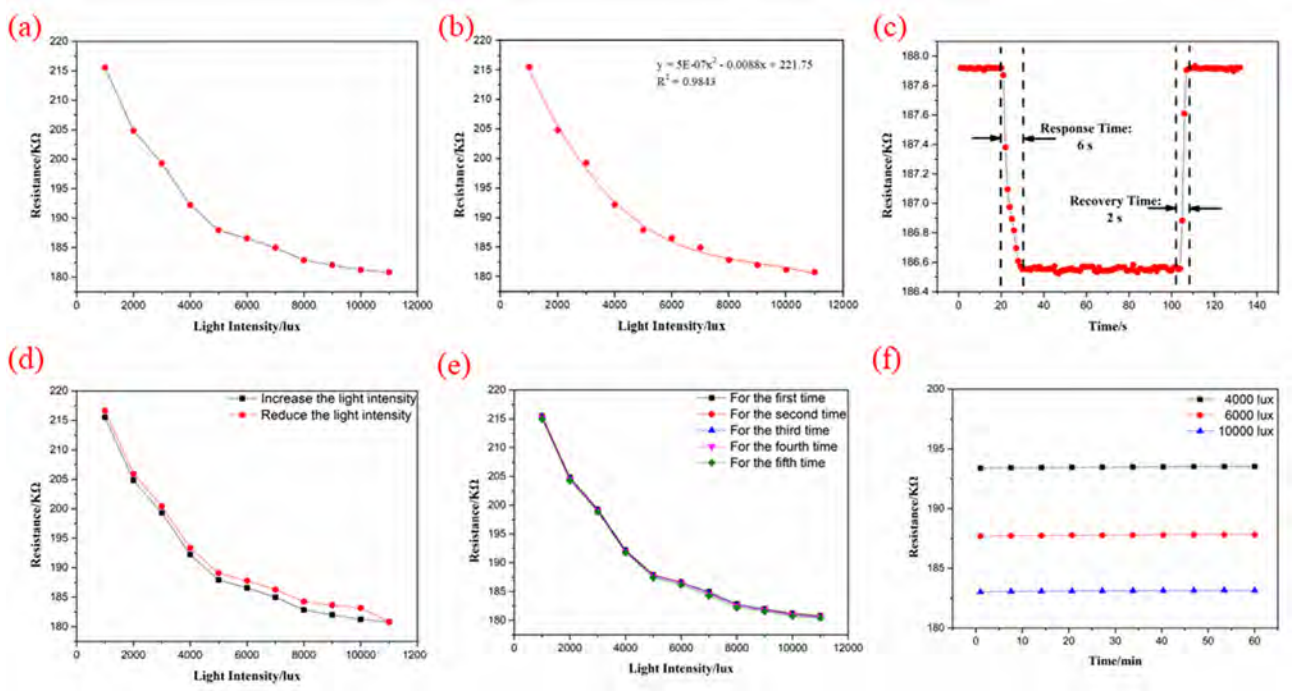


**Fig 5 – (a) Photosensitive sensor resistance characteristic diagram; (b) photosensitive sensor data fitting diagram; (c) response and recovery time test diagram; (d) light intensity hysteresis test diagram; (e) repeatability test diagram; (f) stability test picture.**

inversely correlated with the temperature. Here, we define the hysteresis error as:

$$r = \Delta H_{max} \Big/ y_{fs}$$

where $\Delta H_{max}$ is the maximum deviation value of the output; $y_{fs}$ is the output value under full scale. According to the calculation, it can be concluded that the hysteresis error of the temperature sensor is as small as 4.18%. The starting temperature was set to 10 °C, the ending temperature was set to 60 °C, the resistance value was recorded every second, and 10 samples were taken at the same interval. The performance curve is shown in Fig. 4(e). It can be seen from the figure that after five experiments, the initial resistance decreases, but it basically maintains a linear change. Put the sensor in the environment of 20 °C, 30 °C and 50 °C for 1 h, record the value every 30 s, and sample 10 values to get the resistance change of the sensor within 1 h, as shown in Fig. 4(f). It can be seen from the figure that the fluctuation of the resistance value of the graphene temperature sensor is very small under different temperature environments, which shows that the temperature sensor has good stability.

The light-sensitive material used in this paper is $TiO_2$/G During the test, the temperature-sensitive properties of $TiO_2$, G, $TiO_2$/G (5:1) and $TiO_2$/G (10:1) were tested respectively. The results are shown in the Fig. 3(b), it can be seen that $TiO_2$/G (10:1) has good photosensitivity. The sensing performance of the $TiO_2$/G composite photosensitive sensor was tested. Fig. 5(a) shows the curve of the resistance of the prepared electrode as a function of light intensity. It can be seen from the figure that the $TiO_2$/G photoresistor has a certain conductivity. The resistance value is on the order of $10^4$. It shows that graphene plays a role in improving the conductivity of the thermistor. With the increase of light intensity, the resistance of $TiO_2$/G composites decreased gradually. It can be seen from the figure that the change of the resistance of the electrode is consistent with the change of the light intensity, and both show a downward trend. It starts to slow down at 5000 lux and basically tends to a linear relationship. It shows that the $TiO_2$/G photosensitive sensor has practical application potential. Fig. 5(b) is the data fitting diagram of the photosensitive sensor. The fitting formula of the photosensitive sensor is $y = 5E\text{-}07 \times ^2 - 0.0088x + 221.75$, the correlation coefficient $R^2 = 0.9843$, the response time from 5000 lux to 6000 lux is 6 s, and the recovery time is 2 s (Fig. 5(c)). As the light intensity changes, photoconductivity occurs in photosensitive materials. The optical word energy exceeds the band gap energy of the sensitive material, so that the electrons located on the valence band jump to the conduction band, causing the conduction band of the sensitive material to generate free electrons and the valence band to leave holes, the concentration of carriers inside the sensitive material increases, the conductivity is increased, and the conductivity is increased, which in turn causes resistance changes [36]. Fig. 5(d) shows the hysteresis characteristics of the $TiO_2$/G composite photosensitive sensor. The resistance change curve of the experiment is used for comparison. The black square represents the process of increasing the light intensity, and the red circle represents the process of reducing the light intensity. It can be seen from the figure that the resistance of the photosensitive sensor changes regularly in the process of increasing and decreasing the light intensity. Place the sensor in a closed

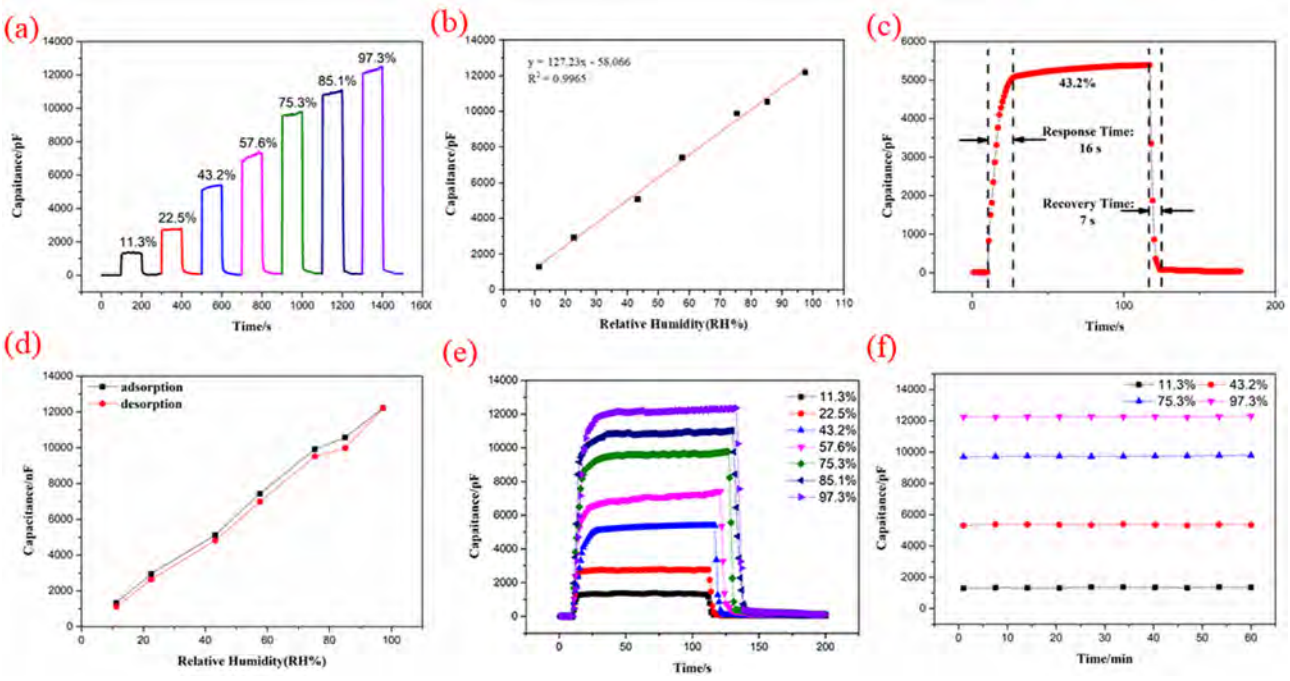


**Fig 6 – (a) Humidity sensor capacitance characteristic diagram; (b) Humidity sensor data fitting diagram; (c) Response and recovery time test diagram; (d) Humidity hysteresis test diagram; (e) Repeatability test diagram; (f) Stability test picture.**

environment from the dark state to the bright state, record the resistance value every second, and finally extract 10 samples at the same interval, repeat the test five times in total, and finally obtain the $TiO_2$/G composite photosensitive sensor repeatability curve, such as Fig. 5(e). It can be seen from the figure that after five experiments, the initial resistance decreases, and it basically maintains a linear change after 5000 lux. Put the sensor in the environment of 4000 lux, 6000 lux and 10,000 lux for 1 h, record the value every 30 s, and sample 10 values to get the resistance change of the sensor within 1 h, as shown in Fig. 5(f). It can be seen from the figure that under different light intensity environments, the fluctuation of the resistance value of the graphene photosensitive sensor is very small, and the visible photosensitive sensor has good stability.

The humidity-sensitive material selected in this paper is $SnO_2$/G. During the test, $SnO_2$, G, $SnO_2$/G (5:1) and $SnO_2$/G (10:1) were tested for temperature-sensitive performance. The results are shown in the figure. As shown in Fig. 3(c), it can be seen that $SnO_2$/G (10:1) has good moisture-sensing properties. The $SnO_2$/G humidity sensor was placed on top of the desiccant for drying, and then placed on top of different saturated salt solutions to test the change of its capacitance value. When it was stable, take it out and put it back in the desiccant for drying. Fig. 6(a) shows the capacitive response of the sensor switching in different humidity environments. It can be seen from the figure that the sensor capacitance is positively correlated with humidity. The capacitance value increases with the increase of humidity and decreases with the decrease of humidity, the response curves under various humidity are relatively complete. For unification, the sensitivity S of the humidity sensor in this paper is defined as:

$$S = \frac{\Delta x}{C_H - C_0}$$

In the formula, $\Delta x$ represents the variation range of humidity in the environment; $C_H$ represents the stable capacitance value of the sensor in different humidity environments; $C_0$ represents the capacitance value of the sensor in the drying environment of the desiccant. The sensitivities under different humidity environments are 0.081, 0.103, 0.086, 0.088, 0.089, 0.092 RH%/pF, respectively. It can be clearly seen that the sensitivity of the sensor is relatively low in a low humidity environment (11.3%), on the contrary, in a high humidity environment (97.3%), the sensitivity of the sensor becomes very large. Its capacitance value varies from 1310 pF to 12,480 pF. Fig. 6(b) is the fitting graph of the humidity sensor data, the fitting formula is $y = 127.23x - 58.066$, and the correlation coefficient $R^2 = 0.9965$. The sensor response and recovery time can be defined as the time it takes for the sensor capacitance to change from the initial value to 90% of the stable deviation. With the change of humidity, the number of water molecules adsorbed between moisture-sensitive materials will change accordingly, which in turn causes changes in the dielectric constant of the material, and eventually leads to a change in capacitance. As shown in Fig. 6(c), the response time under 43.2% humidity environment is selected separately. The calculation of the change time shown in the figure starts when the capacitance value changes to 10% of the stable

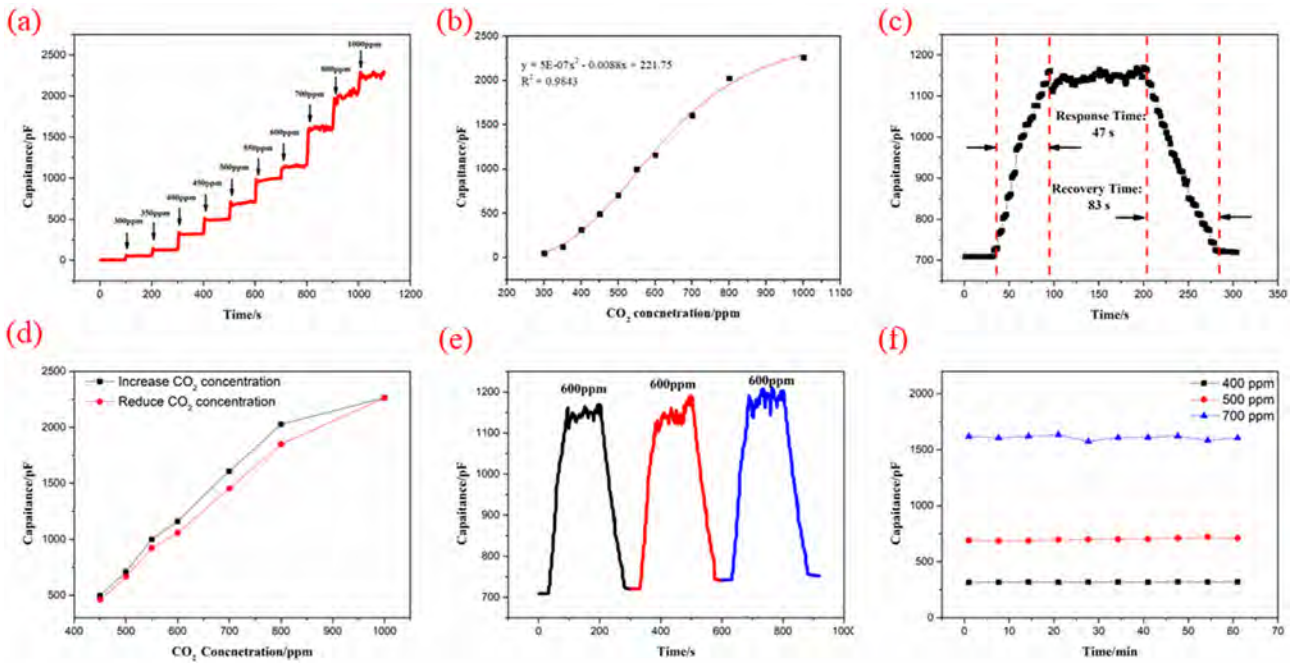


**Fig 7 – (a) Gas sensor resistance characteristic diagram; (b) gas sensor data fitting diagram; (c) response and recovery time test diagram; (d) $CO_2$ gas hysteresis test diagram; (e) repeatability test diagram; (f) Stability test chart.**

value and ends when the capacitance value changes to 90% of the stable value. From this calculation, the response time and recovery time of the sensor in the 43.2% humidity environment are 16 s and 7 s, respectively [37]. It shows that the response time and recovery time of the sensor are in the ideal range. The hysteresis characteristic of the sensor is composed of the moisture absorption and dehumidification characteristic curves of the sensor. Fig. 6(d) shows the hysteresis characteristics of the $SnO_2$/G humidity sensor. The sensor is gradually switched from a low humidity environment to a high humidity environment, respectively, and the upward adsorption curve of the thin film element from low humidity to high humidity is obtained. The environment was switched to a low humidity environment, and a descending desorption curve of the thin film element from high humidity to low humidity was obtained. It can be seen from the figure that the capacitance of the $SnO_2$/G thin film electrode has changed regularly during the upward adsorption of water vapor and the downward desorption of water vapor, both of which are positively correlated with the humidity. The two curves are close, and the humidity is the difference of 85.1% was the largest, and then gradually decreased. In the humidity test experiment, choosing an appropriate time interval is beneficial to study the response recovery characteristics and repeatability of the sensor. In order to explore the repeatability of the $SnO_2$/G humidity sensor, the 11.3 %RH - 97.3 %RH environment was selected to test its repeated response characteristics. The repetitive response curve is shown in Fig. 6(e). It can be seen from the figure that the electrode has good repeatability and stability. Fig. 6(f) shows the long-term stability test of the $SnO_2$/G humidity sensor in a humidity environment of 11.3%, 43.2%, 75.3% and 97.3 %RH, respectively. It can be found that the capacitance of the humidity sensor is basically stable within 60 min.

The gas-sensitive material selected in this paper is $MoS_2$/G. During the test, the temperature-sensitive properties of $MoS_2$, G, $MoS_2$/G (5:1) and $MoS_2$/G (10:1) were tested respectively, and the results are shown in the Fig. 3(d), it can be seen that $MoS_2$/G (10:1) has good gas sensing properties. Put the $MoS_2$/G gas sensor in a closed environment and use a vacuum pump to evacuate the air during the period, and then control the change of the capacitance value by controlling the reaction of different amounts of dilute hydrochloric acid and $CaCO_3$ to prepare $CO_2$. When it is stable, continue to inject dilute hydrochloric acid to increase $CO_2$ concentration. Fig. 7(a) shows the capacitive response of the sensor switching in different $CO_2$ concentration environments. It can be seen from the figure that the sensor capacitance is positively correlated with the $CO_2$ concentration, and the capacitance value increases with the increase of the $CO_2$ concentration. The response curves below are relatively complete. Under each $CO_2$ concentration the response curves are relatively complete. The sensor response and recovery time can be defined as the time it takes for the sensor capacitance to change from the initial value to 90% of the stable deviation. Take the data in steady state for fitting, the fitting diagram of the gas sensor is shown in Fig. 7(b), the fitting formula is $y = -0.002 \times {}^{2} + 6.0647x$ - 1736.4, and the correlation coefficient $R^2 = 0.984$. At the same time, the response time in an environment with a $CO_2$ concentration of 600 ppm was selected separately. The calculation of the change time shown in the figure starts when the capacitance value changes to 10% of the stable value and ends when the capacitance value changes to 90% of the stable value. From this calculation, the response time and recovery

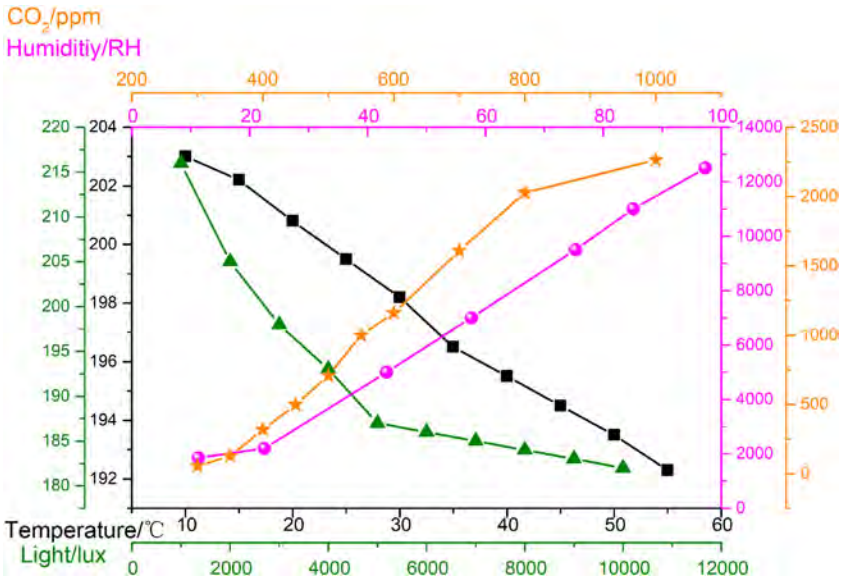


**Fig 8 – The prepared sensor measurement result diagram for the four parameters.**

time of the sensor in an environment with a $CO_2$ concentration of 600 ppm are 47 s and 83 s, respectively (Fig. 7(c)). As the $CO_2$ concentration changes, capacitive $CO_2$ sensors cause changes in circuit capacitance by preferentially adsorbing $CO_2$, and the capacitor is composed of electrode-sensitive materials, and the electrode film thickness is negligible relative to the electrode width and gap spacing. Coating the electrodes with a gas-sensitive material can be used to absorb $CO_2$ gases. When $CO_2$ gas is absorbed into the micropores of permeable solids, the effective permittivity of the film/gas differs from the dielectric constant of the thin film in a vacuum [38]. In order to study the hysteresis effect of the gas sensor, we added $CO_2$ to the confined space in the normal environment, then opened it to interact with the indoor ambient air, and tested its hysteresis (Fig. 7(d)). It can be seen that the initial decline Obviously, this is because the $CO_2$ concentration in the closed environment is too high and the effect is obvious when it interacts with the environment, and the difference decreases when it approaches the atmospheric content. In the gas-sensing test experiment, choosing an appropriate time interval is beneficial to study the response recovery characteristics and repeatability of the sensor. In order to explore the repeatability of the $MoS_2$/G $CO_2$ sensor, the repeated response characteristics were tested in an environment with a $CO_2$ concentration of 600 ppm, and the electrode was switched back and forth three times in an environment with a $CO_2$ concentration of 600 ppm, and the repeated response curve was obtained as shown in Fig. 7(e) shown. It can be seen from the figure that the electrodes have good repeatability. Fig. 7(f) shows the long-term stability test of the $MoS_2$/G $CO_2$ sensor in an environment with a $CO_2$ concentration of 400 ppm, 500 ppm, and 700 ppm, respectively. It can be found that the capacitance of the $CO_2$ sensor is basically stable within 60 min. Finally, we measured the sensors of all four parameters simultaneously in an environment that simulated an agricultural greenhouse, and the results are shown in Fig. 8. The results show that the sensor prepared in this experiment can measure four environmental parameters at the same time.

## 4. Conclusion

In conclusion, a graphene-based low-cost and integrated multi-dimensional sensor is developed in this paper, and the nano-sensitive materials of vegetation have been fully characterized by various structural topography and optical characterization instruments. Through the measurement of the electrode, it is found that its resistance and capacitance have a fast response speed, and the repeatability and stability experiments show that the sensitive material used for the multi-parameter sensor can be reused and has stable performance. The experimental results show that using metal oxides as sensitive materials to fabricate multi-parameter sensors not only facilitates data acquisition, but also reduces manufacturing costs. It can be seen that graphene-based multi-parameter sensors can be devoted to the development of agricultural informatization.

## Declaration of competing interest

The authors declare that they have no known competing financial interests or personal relationships that could have appeared to influence the work reported in this paper.

## Acknowledgements

We would like to thank the Engineering Research Center of Agricultural Multi-Dimensional Sensor Information Perception, Heilongjiang Province, and Heilongjiang Provincial Key Laboratory of Micro-Nano Sensor Component. This work was

jointly supported by university Nursing Program for Young Scholars with Creative Talents in Heilongjiang Province (Grant No. UNPYSCT-2016087), the Heilongjiang Higher Education Teaching Reform Project of Heilongjiang Provincial Department of Education(No. SJGY20200781), Key research and development project of Heilongjiang Province (Nos. GZ20210073 and GZ20210079), Open project of Heilongjiang Key Laboratory of micro nano sensors (No. WNCGQJKF202105), Fundamental Research Funds in Heilongjiang Provincial Universities (No.145109215), and Heilongjiang Science Foundation Project (ZD2019F004).

## Appendix A. Supplementary data

Supplementary data to this article can be found online at https://doi.org/10.1016/j.jmrt.2022.12.157.

## REFERENCES

[1] Thompson NM, DeLay ND, Mintert JR. Understanding the farm data lifecycle: collection, use, and impact of farm data on US commercial corn and soybean farms. Precis Agric 2021;22(6):1685–710.
[2] Dobrota CT, Carpa R, Butiuc-Keul A. Analysis of designs used in monitoring crop growth based on remote sensing methods. Turk J Agric For 2021;45(6):730–42.
[3] Rao Z, Yuan J. Data mining and statistics issues of precision and intelligent agriculture based on big data analysis. Acta Agr Scand B - S P 2021;71(9):870–83.
[4] Kim YS, Kim DH, Chung SO, Choi CH, Choi TH, Kim YJ. Development of an environment field monitoring system to measure crop growth. KJOAS 2019;46(1):57–65.
[5] Syed Khasim, Pasha4 Apsar, Badi Nacer, Lakshmi Mohana, Al-Ghamdi SA, AL-Aoh Hatem A. PVA treated PEDOT-PSS: $TiO_2$ nanocomposite based high-performance sensors towards detection of relative humidity and soil moisture content for agricultural applications. J Polym Environ 2020;29(2):612–23.
[6] Zhao Lin, Wang Jiqiang, Li Zhen, Hou Moyu, Dong Guofeng, Liu Tongyu, Sun Tong, Grattan Kenneth TV. Quasi-distributed fiber optic temperature and humidity sensor system for monitoring of grain storage in granaries. IEEE Sensor J 2020;20(16):9226–33.
[7] Wajid A, Arif Tahir M, et al. Humidity and temperature dependent characteristics of Ag/$SnNcCl_2$/Ag surface type multifunctional sensor. Surf Rev Lett 2020;27(5):1–7.
[8] Karimov KS, Ahmad Z, Khan MI, et al. Elastic layered rubber-graphene composite fabricated by rubbing -in technology for the multi-functional sensors. Heliyon 2019;5(1).
[9] Gupta Shobhnath P, Pawbake Amit S, Sathe Bhaskar R, Late Dattatray J, Walke Pravin S. Superior humidity sensor and photodetector of mesoporous ZnO nanosheets at room temperature. Sensors Actuat B-Chem 2019;293:83–92.
[10] Zhao Y, Yang B, Liu J. Effect of interdigital electrode gap on the performance of $SnO_2$ -modified $MoS_2$ capacitive humidity sensor. Sensors Actuat B-Chem 2018;271:256–63.
[11] Chen X, Mao SS. Titanium dioxide nanomaterials: synthesis, properties, modifications, and applications. ChemInform 2007;38(7):2891.
[12] Xue Shirui, Cao Sicheng, Huang Zhaoling, Yang Daoguo, Zhang Guoqi. Improving gas-sensing performance based on MOS nanomaterials: a review. Materials 2021;14(15):4263.
[13] Luo Jiajia, Liu Gui-Shi, Zhou Wenjian, Hu Shiqi, Chen Lei, Chen Yaofei, Luo Yunhan, Chen Zhe. A graphene–PDMS hybrid overcoating enhanced fiber plasmonic temperature sensor with high sensitivity and fast response. J Mater Chem C 2020;8(37):12893–901.
[14] Meng Fanli, Yu Yao, Yuan Zhenyu, Qi Tianyao, Li Jin. Room-temperature NH3 sensors based on boron-doped graphene oxide: enhanced sensing performance by BN covalent interaction. IEEE Trans Nanotechnol 2021;20:726–32.
[15] Yao Y, Xue Y. Influence of the oxygen content on the humidity sensing properties of functionalized graphene films based on bulk acoustic wave humidity sensors. Sensor Actuat B-Chem 2016;222:755–62.
[16] Huang JianRen, Yang XiaoXiang, Her Shiuh-Chuan, Liang Yuan-Ming. Carbon nanotube/graphene nanoplatelet hybrid film as a flexible multifunctional sensor. Sensors-Basel 2019;19(2):317. 317.
[17] Yun Oh Seung, Hong Soo Yeong, Jeong Yu Ra, Yun Junyeong, Park Heun, Jin Sang Woo, Lee Geumbee, Oh Ju Hyun, Lee Hanchan, Lee Sang-Soo, Jeong Sook Ha. Skin-attachable, stretchable electrochemical sweat sensor for glucose and pH detection. ACS appl mater inter 2018;10(16):13729–40.
[18] Gupta Shobhnath P, Pawbake Amit S, Sathe Bhaskar R, Late Dattatray J, Walke Pravin S. Superior humidity sensor and photodetector of mesoporous ZnO nanosheets at room temperature. Sensor Actuat B-Chem 2019;293:83–92.
[19] Mahmod WE, Al-Bluwi SA. Development of highly sensitive temperature sensor made of graphene monolayers doped P(VDF-TrFE) nanocomposites. Sensor Actuat A-Phys 2020;312:112101.
[20] Rosace Giuseppe, Trovato Valentina, Colleoni Claudio, Caldara Michele, Re Valerio, Brucale Marco, Piperopoulos Elpida, Mastronardo Emanuela, Milone Candida, De Luca Giovanna, RosariaPlutino Maria. Structural and morphological characterizations of MWCNTs hybrid coating onto cotton fabric as potential humidity and temperature wearable sensor. Sensor Actuat B-Chem 2017;252:428–39.
[21] Leonardi SG, Wlodarski W, Li Y, Donato N, Sofer Z, Pumera M, Neri G. A highly sensitive room temperature humidity sensor based on 2D-WS2 nanosheets. Flatchem 2018;9:21–6.
[22] MariaO' Brien, Lee Kangho, Morrish Rachel, Berner Nina C, McEvoy Niall, Wolden Colin A, Duesberg Georg S. Plasma assisted synthesis of WS2 for gas sensing applications. Chem Phys Lett 2014;615:6–10.
[23] Kebabian PL, Freedman A. Fluoropolymer-based capacitive carbon dioxide sensor. Meas Sci Technol 2006;17(4):703–10.
[24] Duan Z, Zhao Q, Wang S, et al. Halloysite nanotubes: natural, environmental-friendly and low-cost nanomaterials for high-performance humidity sensor. Sensor Actuat B-Chem 2020;317:128204.
[25] Zhang Dongzhi, Sun Yan'e, Peng Li, Zhang Yong. Facile fabrication of $MoS_2$ -modified $SnO_2$ hybrid nanocomposite for ultrasensitive humidity sensing. Acs Appl Mater Inter 2016;8(22):14142–9.
[26] Song Z, Zhang J, Jiang J. Morphological evolution, luminescence properties and a high-sensitivity ethanol gas sensor based on 3D flower-like $MoS_2$–ZnO micro/nanosphere arrays. Ceram Int 2019;46(5):6634–40.
[27] Yusuf V, Kaneti,Yue J, et al. Experimental and theoretical studies on noble metal decorated tin oxide flower-like nanorods with high ethanol sensing performance. Sensor Actuat B-Chem 2015;219:83–93.
[28] Xing Chengcheng, Zhang Dan, Cao Ke, Zhao Shumin, Wang Xin, Qin Haiying, Liu Jiabin, Jiang Yinzhu, Meng Liang.

In situ growth of FeS microsheet networks with enhanced electrochemical performance for lithium-ion batteries. J Mater Chem 2015;3(16):8742–9.
[29] Arya S, Sonawane H, Math S, et al. Biogenic titanium nanoparticles (TiO2NPs) from Tricoderma citrinoviride extract:synthesis,characterization and antibacterial activity against extremely drug-resistant Pseudomonas aeruginosa. Int Nano Lett 2021;11(1):35–42.
[30] Madhavi V, Kondaiah P. Influence of silver nanoparticles on titanium oxide and nitrogen doped titanium oxide thin films for sun light photocatalysis. Appl Surf Sci 2018;436:708–19.
[31] Aslam M, Qamar MT, Ali S, et al. Evaluation of $SnO_2$ for sunlight photocatalytic decontamination of water. J Environ Manag 2018;217:805–14.
[32] Zhang D, Chang H, Peng L, et al. Fabrication and characterization of an ultrasensitive humidity sensor based on metal oxide/graphene hybrid nanocomposite. Sensor Actuat B-Chem 2016;225:233–40. MAR.
[33] Ali G, Thalji MR, Soh WC, et al. One-step electrochemical synthesis of MoS2/graphene composite for supercapacitor application. J Solid State Electrochem 2020;24(1):25–34.
[34] Su L, Luo L, Wang J, et al. Lamellar flower-like porous $MoS_2$ as an efficient cocatalyst to boost photocatalytic hydrogen evolution of CdS. Catal Sci Technol 2021;11(4):1292–7.
[35] Shen T, Dai X, Li B, et al. ZnO composite graphene as sensing coating for interferometric temperature sensor. J Phys D Appl Phys 2020;53(34):345401.
[36] Ding L, Liu N, Li L, et al. Graphene-skeleton heat-coordinated and nanoamorphous-surface-state controlled pseudo-negative-photoconductivity of tiny $SnO_2$ nanoparticles. Adv Mater 2015;27(23):3525–32.
[37] Shin G. Soft, wirelessly powered humidity sensor based on $SnO_2$ nanowires for wireless/wearable sensor application. Materials 2020;13(9):2176.
[38] Wang Z, Zhi M, Xu M, et al. Ultrasensitive $NO_2$ gas sensor based on Sb-doped $SnO_2$ covered ZnO nano-heterojunction. J Mater Sci 2021;56(12):7348–56.

# Appendix A. Supplementary data

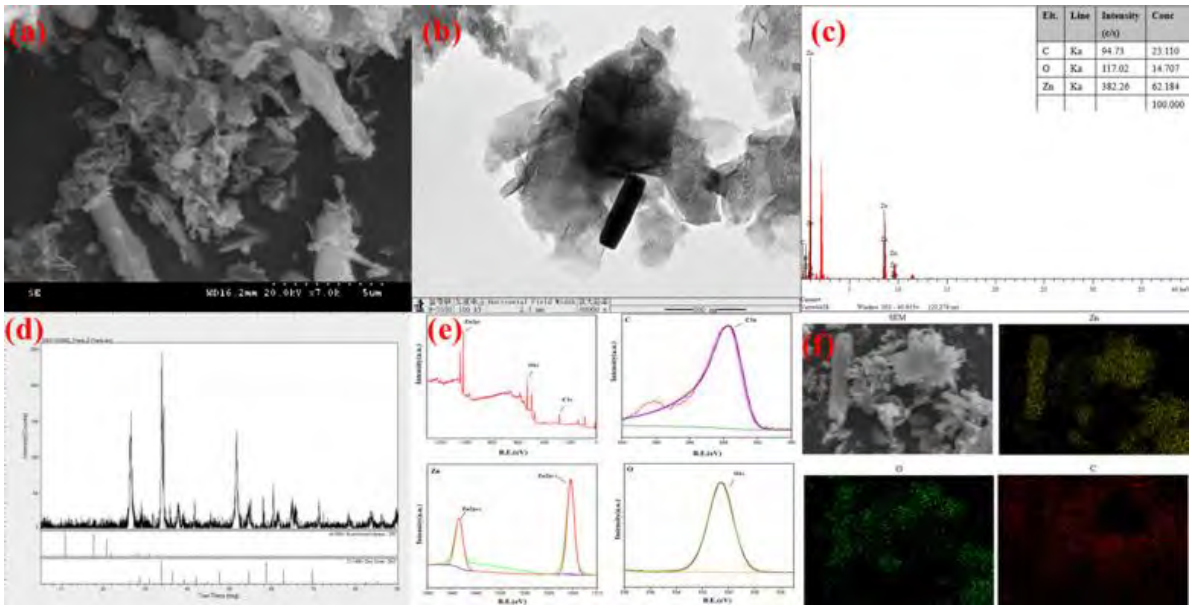


Supporting material 1. **(a)** Scanning electron microscope image of thermosensitive material ZnO; **(b)** TEM image; **(c)** EDS spectrum; **(d)** XRD pattern; **(e)** XPS full spectrum and single spectrum of each element; **(f)** Element mapping diagram.

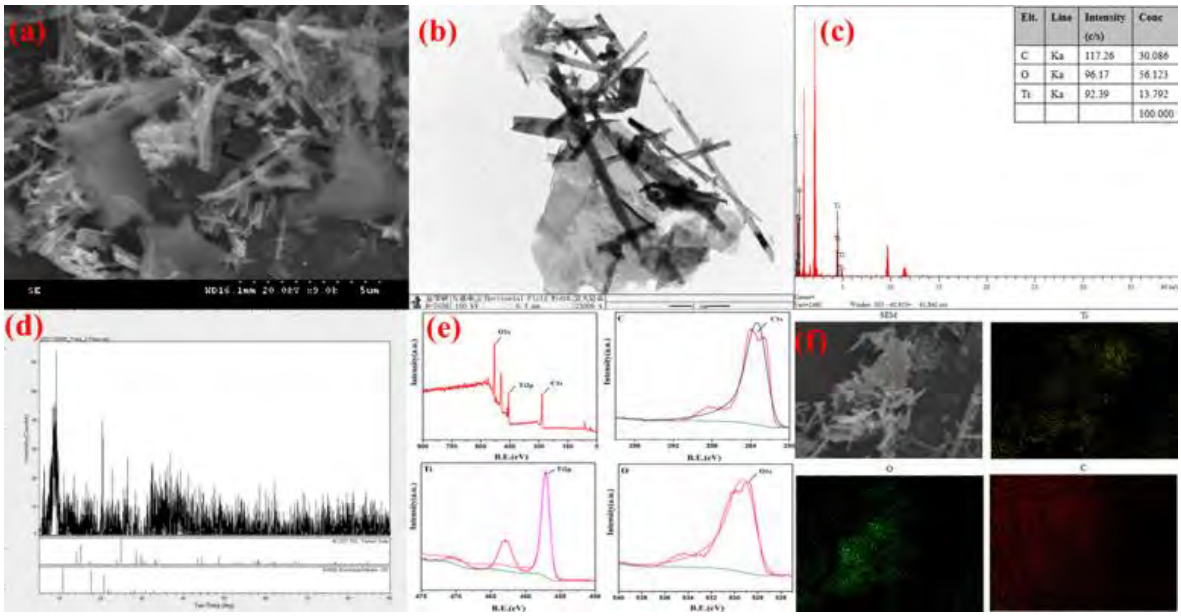


Supporting material 2. **(a)** Scanning electron microscope image of the photosensitive material $TiO_2$; **(b)** TEM image; **(c)** EDS spectrum; **(d)** XRD pattern; **(e)** XPS full spectrum and single spectrum of each element; **(f)** mapping map of each element.

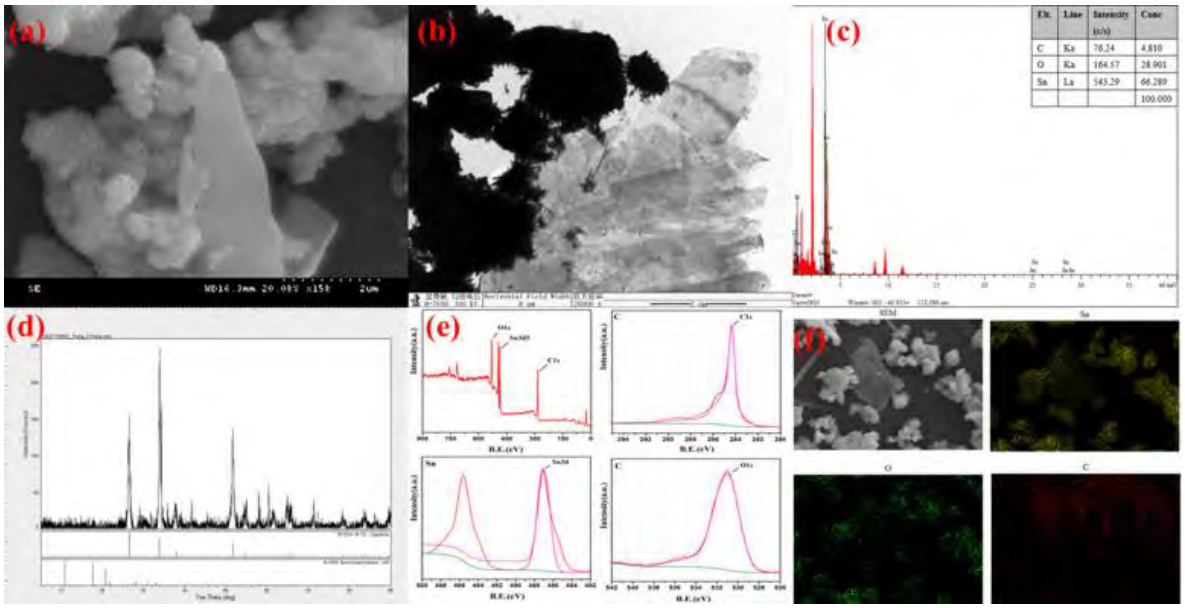


Supporting material 3. **(a)** SEM image of humidity-sensitive material $SnO_2$; **(b)** TEM image; **(c)** EDS spectrum; **(d)** XRD pattern; **(e)** XPS full spectrum and single spectrum of each element; **(f)** Element mapping diagram.

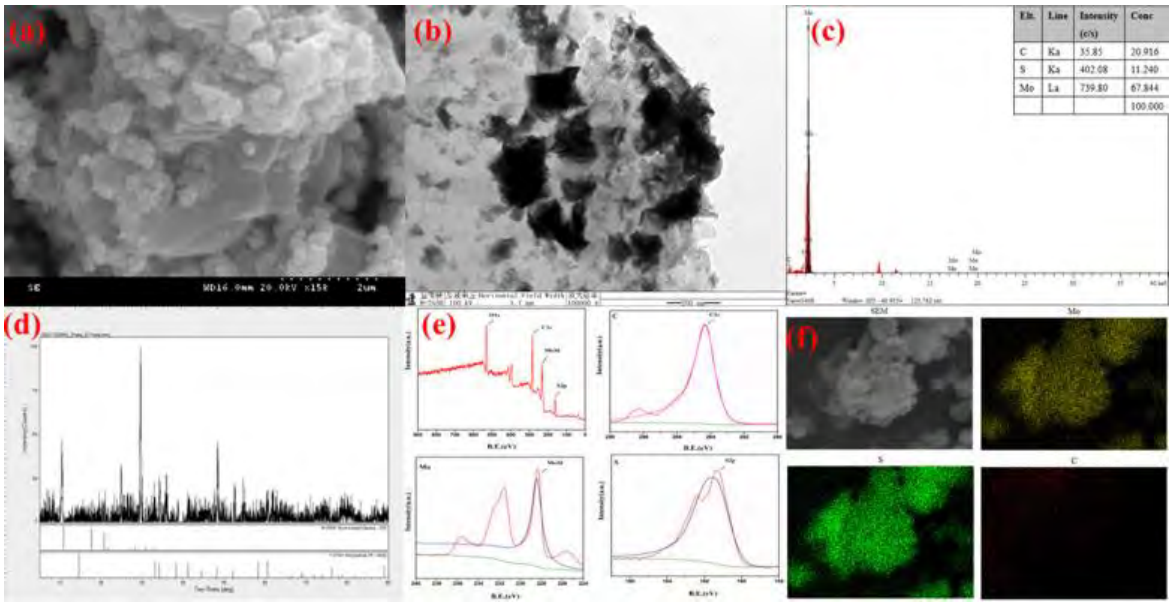


Supporting material 4. **(a)** SEM image of gas-sensitive material $MoS_2$; **(b)** TEM image; **(c)** EDS spectrum; **(d)** XRD pattern; **(e)** XPS full spectrum and single spectrum of each element; **(f)** mapping of each element.